

## Higher-order topological superconductors based on weak topological insulators

Xun-Jiang Luo, Xiao-Hong Pan, and Xin Liu<sup>✉\*</sup>

*School of Physics and Institute for Quantum Science and Engineering, Huazhong University of Science and Technology,  
Wuhan, Hubei 430074, China  
and Wuhan National High Magnetic Field Center and Hubei Key Laboratory of Gravitation and Quantum Physics,  
Wuhan, Hubei 430074, China*



(Received 2 April 2021; revised 31 August 2021; accepted 8 September 2021; published 22 September 2021)

Higher-order topological phases host robust boundary states at the boundary of the boundary, which can be interpreted from their boundary topology. In this work, we show that based on the surface states of a weak topological insulator, the interplay between superconductors and magnetic fields can lead to the various helical or chiral Majorana hinge modes and even corner modes. Particularly, the obtained higher-order topological superconductors (TSCs) can be attributed to their certain boundaries, surfaces, or hinges, which naturally behave as a TSC in DIII or D symmetry class. Correspondingly, these higher-order TSCs can be characterized by the boundary topological invariants, such as surface Chern numbers or surface  $Z_2$  topological invariants for surface TSCs. Remarkably, some chiral hinge states naturally form the Majorana interference loop without complicated heterostructure, revealing the exceptional property of higher-order TSCs. Our models not only can be realized in iron-based superconductors with desired inverted band structures and superconducting pairings, but also pave the way to the implementation of quantum interference device from the higher-order topological matters.

DOI: [10.1103/PhysRevB.104.104510](https://doi.org/10.1103/PhysRevB.104.104510)

### I. INTRODUCTION

Topological insulators (TIs) and topological superconductors (TSCs) feature gapless boundary states protected by bulk topological property, which can be characterized by topological invariants defined throughout the Brillouin zone [1,2]. For concreteness, three-dimensional (3D) TIs with time-reversal symmetry are known to be characterized by one strong and three weak  $Z_2$  topological indices [3,4]. According to these four  $Z_2$  indices, two classes of TIs can be distinguished, strong TIs and weak TIs, which host an odd and even number of Dirac cones on surfaces, respectively. Remarkably, the findings of strong TIs [5–7] provide the parent materials of laboratory achievable TSCs. Several strong TI-based experimental platforms to realize TSCs have been proposed by taking advantage of the spin-momentum locking property of surface states of strong TIs [8–12]. To be specific, Majorana zero modes can be realized by performing the Fu-Kane scheme [8], which considers the  $\pi$  flux vortex of the surface states with  $s$ -wave pairing. Moreover, chiral TSCs hosting chiral Majorana modes can be realized by considering magnetic TI thin-film proximity to  $s$ -wave superconductor [11,12]. The interplay between magnetic fields and superconductors to gap the surface states of strong TIs tremendously enriches the field of TSCs for their creation, detection, and manipulation [13–17]. Meanwhile, this also naturally raises the following question: Can weak TIs, hosting more abundant surface states, be utilized to realize TSC?

On the other hand, the concept of topological phases has been generalized to higher order over the past few years,

which has been drawing great research interest as new topological phases of matter [18–40]. Generally, an  $n$ th-order topology in the dD system manifests itself by localized states at its (d-n)D boundaries. For instance, second- and third-order topological phases of a 3D system feature hinge modes and corner modes, respectively. In this classification scheme, conventional topological phases are the first order in nature. A prototypical method of obtaining higher-order topological phases is to gap adjacent gapless boundary states in a nontrivial way, giving rise to boundary topological defects [30–38]. This scenario is soon applied to realize the higher-order TSC by considering the gapless boundary states of strong TIs in two dimensions (2D) or 3D, which can be gapped by superconductors breaking U(1) symmetry or Zeeman fields breaking time-reversal symmetry. Correspondingly, the boundary domain walls, which can be generated by opposite superconducting gaps [41–45], or magnetic-superconducting gaps [46–53] along adjacent boundaries, will lead to Majorana corner or hinge modes. Meanwhile, the implementation of higher-order TSC based on weak TI is seldom studied [54].

In this work, we start from weak TIs rather than strong TIs to design second- and third-order TSCs hosting robust Majorana hinge modes and Majorana corner modes (MCMs), respectively. Concretely, we consider weak TIs with band inversion at both  $\Gamma(0, 0, 0)$  and  $Z(0, 0, \pi)$  points in Brillouin zone. For this phase, the surface Dirac cones only appear on side faces and their number is two. We find that second-order TSC hosting helical Majorana hinge modes (HMHMs) can be realized in this system by considering  $s_{\pm}$ -wave superconductivity to gap the Dirac cones on the side faces. Through the topological analysis of surfaces, we show that the corresponding side faces of this system naturally behave as a time-reversal invariant TSC (TRITSC), characterized by

\*phyliuxin@hust.edu.cn

a surface  $Z_2$  topological invariant. Moreover, in the presence of an in-plane Zeeman field, the side faces can be selectively driven to a chiral TSC through a surface topological phase transition, giving rise to chiral Majorana hinge modes (CMHMs), which is characterized by nontrivial surface Chern number. Interestingly, the tunability of the CMHMs allows the formation of the Majorana interference loop on the (001) surface, which is not only useful for the detection of hinge modes but also indicates the great potential of building quantum device from the higher-order topological matter without complicated heterostructures. Analogously, third-order TSC can be realized by designing a one-dimensional (1D) hinge TSC. We propose a theoretical model to realize third-order TSC through this visualized principle and provide topological characterizations. For candidate material, our model can effectively capture the topological property of iron-based superconductor Li(OH)FeSe, whose normal state was predicted to be a weak TI with band inversion at  $\Gamma$  and Z points [55].

## II. SECOND-ORDER TSCs

### A. Model and Hamiltonian

We first introduce the Bogoliubov-de Gennes (BdG) Hamiltonian on a cubic lattice, which describes 3D weak TI with  $s_{\pm}$ -wave superconductor pairing,

$$H_{\text{BdG}}(\mathbf{k}) = \begin{pmatrix} \mathcal{H}(\mathbf{k}) - \mu & -i\Delta(\mathbf{k})s_y \\ i\Delta(\mathbf{k})s_y & -\mathcal{H}^*(-\mathbf{k}) + \mu \end{pmatrix}, \quad (1)$$

with the normal-state Hamiltonian  $\mathcal{H}(\mathbf{k}) = \sum_{j=x,y,z} (m_0 - t_j \cos k_j) \sigma_z s_0 + \sin k_j \sigma_x s_j$ . Here,  $\mu$  is the chemical potential,  $m_0$  and  $t_j$  are taken to be positive model parameters,  $s$  and  $\sigma$  are Pauli matrices in the spin and orbital spaces, respectively. The  $s_{\pm}$ -wave pairing order parameter is  $\Delta(\mathbf{k}) = \Delta_0 + \Delta_1 (\cos k_x + \cos k_y)$ , which can be achieved intrinsically in an iron-based superconductor [56–59].

It is readily verified that  $H_{\text{BdG}}(\mathbf{k})$  respects time-reversal symmetry ( $\mathcal{T} = is_y \mathcal{K}$ ), inversion symmetry ( $I = \sigma_z$ ), and particle-hole symmetry ( $\mathcal{P} = \tau_x \mathcal{K}$ ), where  $\tau$  are Pauli matrices in particle-hole space and  $\mathcal{K}$  denotes the complex conjugation. Thus, the band topology of  $\mathcal{H}(\mathbf{k})$  is easily read off using the Fu-Kane criterion [4] based on the eigenvalues of  $I$  at the eight TRI momenta points. For our purposes, we focus on the region of the parameters, in which the band inversion of  $\mathcal{H}(\mathbf{k})$  occurs at both  $\Gamma$  and Z points in the first Brillouin zone. Constrained into this region, there are no topological surface states on (001) surface while there are two Dirac cones on each side face, crossing at  $k_z = 0$  and  $\pi$ , respectively. For a slab geometry with open boundary condition along the  $x$  direction, the energy spectrum of surface Dirac cones on the (100) surface is shown in Fig. 1(a).

Based on this weak TI, the physical picture of realizing surface TSC can be described as follows. When the chemical potential is inside the bulk electronic band gap, there are two Fermi surfaces around each Dirac cone, as shown in Fig. 1(b). Further considering bulk  $s_{\pm}$ -wave pairing, surface Dirac cones of weak TI, described by 2D massless Dirac fermion, are gapped out by the superconducting pairing, which introduces Dirac mass. Remarkably, different from the case of uniform  $s$ -wave pairing,  $s_{\pm}$  pairing can gap the Dirac cones with dif-

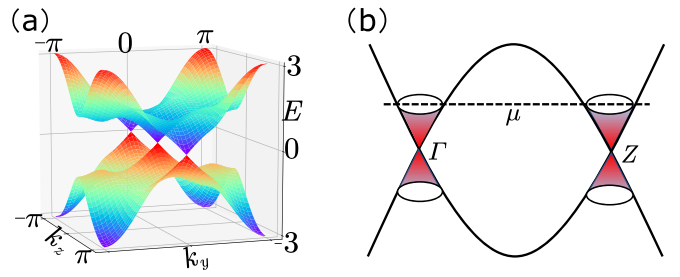


FIG. 1. (a) The energy spectrum of two Dirac cones on the (100) surface is plotted. Model parameters are taken as  $m = 2$ ,  $t_x = t_y = 2$ ,  $t_z = 1$ . (b) Schematic plot of the two Fermi surfaces around the two surface Dirac cones.

ferent magnitudes. Owing to this property, the Dirac masses of the two Dirac cones on the same side face can have a sign change under appropriate parameter condition. In this case, the side face exists an odd number of Fermi surfaces with negative superconducting pairing, which enables the realization of a surface TRITSC [60–62], although the bulk is a trivial superconductor. To demonstrate this simple physical picture, we perform surface theory in the following.

### B. Second-order TSC in DIII symmetry class

For the sake of simplicity, we take  $\mu = 0$  and focus on the continuum model by expanding the bulk Hamiltonian  $H_{\text{BdG}}(\mathbf{k})$  to second order around  $\Gamma$  and Z points, respectively,

$$H_{\text{BdG}}^{\gamma(z)} = [m_{\gamma(z)} + (t_x/2)k_x^2 + (t_y/2)k_y^2 \pm t_z/2k_z^2] \tau_z \sigma_z + k_x \sigma_x s_x + k_y \tau_z \sigma_x s_y \pm k_z \sigma_x s_z + [\bar{\Delta} - \Delta_1/2(k_x^2 + k_y^2)] \tau_y s_y, \quad (2)$$

where bulk electronic band gaps  $m_{\gamma(z)} = m_0 - t_x - t_y \mp t_z < 0$  are taken to ensure that the band inversion of normal state occurs at  $\Gamma$  and Z points simultaneously,  $\bar{\Delta}$  is defined as  $\Delta_0 + 2\Delta_1$ . Without loss of generality, we concentrate on the topology of the (100) surface and take the open boundary condition of the  $x$  direction. Under this condition, we replace  $k_x \rightarrow -i\partial_x$  and then the BdG Hamiltonian can be decomposed as  $H_{\text{BdG}}^{\gamma(z)} = H_0^{\gamma(z)}(x) + H_p^{\gamma(z)}(x, k_y, k_z)$ , in which

$$H_0^{\gamma(z)} = \left( m_{\gamma(z)} - \frac{t_x}{2} \partial_x^2 \right) \tau_z \sigma_z - i\partial_x \sigma_x s_x, \\ H_p^{\gamma(z)} = k_y \tau_z \sigma_x s_y \pm k_z \sigma_x s_z + \Delta(x) \tau_y s_y, \quad (3)$$

where  $\Delta(x)$  is defined as  $\bar{\Delta} + \frac{\Delta_1 \partial_x^2}{2}$  and the irrelevant terms  $k_y^2$  and  $k_z^2$  have been omitted. Now we solve the zero-energy states of  $H_0^{\gamma(z)}$  and consider  $H_p^{\gamma(z)}$  as a perturbation to extract the surface low-energy Hamiltonian.

Solving the eigenequation  $H_0^{\gamma(z)} |\psi_{\alpha}^{\gamma(z)}(x)\rangle = 0$  under the boundary conditions  $|\psi_{\alpha}^{\gamma(z)}(x=0)\rangle = |\psi_{\alpha}^{\gamma(z)}(x=-\infty)\rangle = 0$ , there are four zero-energy states. The wave function of these zero-energy states can be written as

$$|\psi_{\alpha}^{\gamma(z)}(x)\rangle = \mathcal{N}_{\gamma(z)} \sin(\kappa_1^{\gamma(z)} x) e^{\kappa_2 x} |\xi_{\alpha}\rangle, \quad (4)$$

with  $\kappa_1^{\gamma(z)} = \sqrt{2|m_{\gamma(z)}|/t_x - 1/t_x^2}$ ,  $\kappa_2 = 1/t_x$ , and  $\mathcal{N}_{\gamma(z)}$  the normalization factors. Spinor  $|\xi_{\alpha}\rangle$  statisfies  $\tau_z \sigma_x s_x |\xi_{\alpha}\rangle = |\xi_{\alpha}\rangle$ .

We choose them as

$$\begin{aligned} |\xi_1\rangle &= \frac{1}{\sqrt{2}}(|+, +, +\rangle + |-, +, -\rangle), \\ |\xi_2\rangle &= \frac{1}{\sqrt{2}}(|+, -, -\rangle - |-, -, +\rangle), \\ |\xi_3\rangle &= \frac{1}{\sqrt{2}}(|+, -, -\rangle + |-, -, +\rangle), \\ |\xi_4\rangle &= \frac{1}{\sqrt{2}}(|-, +, -\rangle - |+, +, +\rangle), \end{aligned} \quad (5)$$

with  $|z_1, z_2, z_3\rangle = |\tau_z = z_1\rangle \otimes |\sigma_y = z_2\rangle \otimes |s_x = z_3\rangle$ . Projecting  $H_p$  into the subspace spanned by these four zero-energy states, the surface Hamiltonian can be written as

$$\tilde{H}^{\gamma(z)} = k_y \tilde{\tau}_x \tilde{s}_z \pm k_z \tilde{\tau}_y \tilde{s}_0 + \Delta_x^{\gamma(z)} \tilde{\tau}_z \tilde{s}_0, \quad (6)$$

where  $\tilde{\tau}$  and  $\tilde{s}$  are Pauli matrices acting in zero-energy subspace and  $\Delta_x^{\gamma(z)} = \bar{\Delta} + \Delta_1 m_{\gamma(z)}/t_x$  denote the pairing gap magnitude of the Dirac cones on the (100) surface. As a result, the two superconducting gaps  $\Delta_x^\gamma$  and  $\Delta_x^z$  have different magnitudes although the pairing order parameter  $\Delta(\mathbf{k})$  does not depend on  $k_z$ . This is because surface Dirac electrons at  $\Gamma$  and  $Z$  points have different decaying coherence length, determined by the bulk electronic band gaps  $m_{\gamma(z)}$ , which are captured by the pairing potential function  $\Delta(x)$  in the process of projection. Note that the time-reversal symmetry and particle-hole symmetry are intact for surface Hamiltonians  $\tilde{H}^{\gamma(z)}$ , with given by  $\tilde{T} = i\tilde{s}_y \mathcal{K}$ ,  $\tilde{\mathcal{P}} = \tilde{\tau}_x \mathcal{K}$ . Thus, the surface Hamiltonian belongs to DIII symmetry class, which has a  $Z_2$  topological classification [63–65].

Here, although it is not easy to obtain the surface Hamiltonian of the whole Brillouin zone, the topology of the surface BdG Hamiltonian can be fully determined by the sign of the superconducting gap functions  $\Delta_x^{\gamma(z)}$  of the Fermi surfaces around  $\Gamma$  and  $Z$  points. From the phase  $\Delta_x^\gamma \Delta_x^z > 0$  to the phase  $\Delta_x^\gamma \Delta_x^z < 0$ , the surface gap must be closed, indicating a surface topological phase transition. When  $\Delta_x^\gamma \Delta_x^z < 0$ , the (100) surface exists an odd number of Fermi surfaces with negative superconducting pairing. In this case, the (100) surface is expected to be nothing but a TRITSC. Consequently, the topology of the (100) surface can be characterized by the surface  $Z_2$  topological invariant

$$(-1)^{\nu_x} = \text{sgn}(\Delta_x^\gamma \Delta_x^z). \quad (7)$$

The condition  $\nu_x = 1$  indicates the realization of surface TRITSC and it leads to

$$-2 + |m_z|/t_x < \Delta_0/\Delta_1 < -2 + |m_\gamma|/t_x. \quad (8)$$

Thus, the region of topological parameters is proportional to the difference between bulk electronic band gaps  $m_\gamma$  and  $m_z$ , equaling to  $2t_z$ .

When taking the open boundary condition of the  $y$  direction, the low-energy Hamiltonian of (010) surface can be obtained through a similar solving process [66]. This surface Hamiltonian gives rise to the identical physics to that on the (100) surface. Analogously, the topology of the (010) surface can be characterized by the surface  $Z_2$  topological invariant

$$(-1)^{\nu_y} = \text{sgn}(\Delta_y^\gamma \Delta_y^z), \quad (9)$$

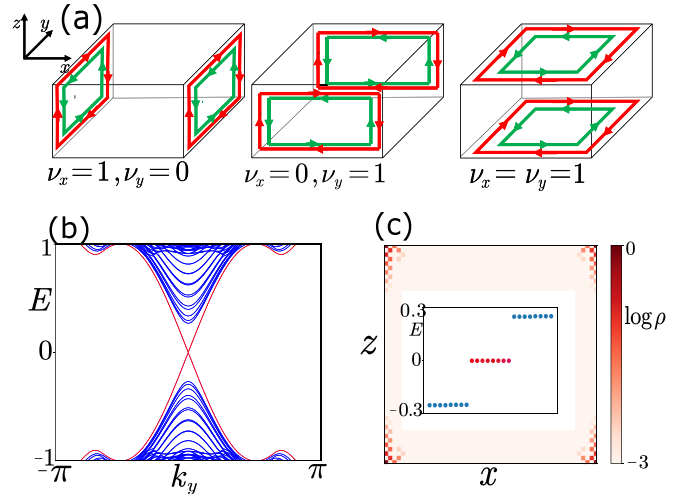


FIG. 2. (a) The distributions of the HMHMs are schematically plotted under the parameters, yielding different surface  $Z_2$  topological invariants  $\nu_x$  and  $\nu_y$ . (b) The energy spectrum of a wire geometry along  $y$  is plotted under the parameters  $m = 2$ ,  $t_x = t_y = 2$ ,  $t_z = 1$ ,  $\Delta_0 = -\Delta_1 = -0.5$ , with which we have  $\nu_x = \nu_y = 1$ . The numerical calculation is performed with the size  $20 \times 20$  of the plane with open boundary condition. The in-gap states are of fourfold degeneracy, which correspond to four pairs of HMHMs. (c) The spatial profile of the MCMs is plotted when  $k_y = 0$  in (b) and the inset plots the energies close to zero. The numerical calculation is performed with the size  $60 \times 60$  of the plane with open boundary condition. The color bar represents the log value of the density  $\rho$  of the Majorana corner states.

with  $\Delta_y^{\gamma(z)} = \bar{\Delta} + \Delta_1 m_{\gamma(z)}/t_y$ , which denote the pairing gap magnitude of the two Dirac cones on the (010) surface. When  $\Delta_y^\gamma \Delta_y^z < 0$ ,  $\nu_y$  takes value 1, which implies that the (010) surface behaves as a TRITSC.

Since 2D TRITSC hosts helical edge Majorana modes and the edge of the surface is the hinge of the 3D system, the surface TRITSC will be manifested by the presence of HMHMs. Therefore, when surface topological invariants  $\nu_x = 1$  and  $\nu_y = 0$ , there are HMHMs localized at the hinges shared by the (100) surface and other surfaces. When surface topological invariants  $\nu_x = 0$  and  $\nu_y = 1$ , there are HMHMs localized at the hinges shared by the (010) surface and other surfaces. Especially, when surface topological invariants  $\nu_x = \nu_y = 1$ , both the (100) and (010) surfaces are TRITSCs. The hinges shared by the (100) and (010) surfaces have two copies  $Z_2$  protected HMHMs, which will couple with each other resulting in no hinge modes. Thus, in this case, there are HMHMs localized at the hinges shared by the (001) surface and other surfaces. In Fig. 2(a), we provide the schematic plot of the HMHMs for these three different cases. In Figs. 2(b) and 2(c), we verify the existence of the HMHMs through numerical calculation for the case  $\nu_x = \nu_y = 1$ . Naturally, the whole system is a second-order TSC in DIII symmetry class due to the existence of HMHMs.

The HMHMs can also be characterized by the winding of the Wilson loop spectrum for a slab geometry [43]. For instance, the HMHMs along  $k_y$  in Fig. 2(b) can be characterized by the winding of the Wannier spectrum along  $k_y$ , obtained

by performing Wilson loop along  $k_x$  for a slab geometry on the (001) surface [66]. This winding of the Wannier spectrum unambiguously signals the existence of HMHMs.

### C. Second-order TSC in D symmetry class

Up to now, the time-reversal symmetry that protects the HMHMs is preserved. When further applying an in-plane magnetic field to break time-reversal symmetry, another interesting surface topological phase transition can occur. Without loss of generality, considering the Zeeman term  $V_x \tau_z s_x$  induced by the magnetic field along the  $x$  direction, the degenerate surface states on (100) surface have Zeeman splitting. Similar to strong TIs, this Zeeman term produces no influence for the surface states on the (010) surface [26,50]. Consequently, the superconducting pairing gaps  $\Delta_x^{\gamma(z)}$  are split to two-gap amplitudes  $|\Delta_x^{\gamma(z)}| \pm |V_x|$ . Obviously, increasing  $V_x$  from zero, the surface gap first decreases to zero at  $\{|\Delta_x^{\gamma}|, |\Delta_x^z|\}_{\min} = |V_x|$  and then reopens with further increasing  $V_x$ . This indicates another surface topological phase transition, which is associated with the gap closing and reopening of the nondegenerate surface Dirac cone. It is known that the Chern number will be changed by one when the energy gap of the massive Dirac cone is closed and reopened [67]. On the other hand, no matter the topological invariant  $v_x = 1$  or 0 in the absence of the magnetic field, the surface Chern number for whole surface bands is zero due to time-reversal symmetry. Thus, in the presence of finite magnetic field, the (100) surface can be driven to surface chiral TSC characterized by a nontrivial surface Chern number.

To verify the above physical picture, we calculate surface Chern number  $C_x$  from low-energy surface Hamiltonian. Directly, the influence of the Zeeman term  $V_x \tau_z s_x$  for surface states can be taken into account by projecting it into the subspace spanned by zero-energy states in Eq. (4). Performing this projection calculation, we obtain an additional term  $V_x \tilde{\tau}_z \tilde{s}_z$ . Thus, the surface Hamiltonians  $\tilde{H}^{\gamma(z)}$  in Eq. (6) transform into the form

$$\tilde{H}^{\gamma(z)} = k_y \tilde{\tau}_x \tilde{s}_z \pm k_z \tilde{\tau}_y \tilde{s}_0 + \Delta_x^{\gamma(z)} \tilde{\tau}_z \tilde{s}_0 + V_x \tilde{\tau}_z \tilde{s}_z. \quad (10)$$

Obviously, the surface Hamiltonians are block diagonal in  $\tilde{s}$  space and each block describes a massive Dirac cone, which has been well known to contribute half Chern number, depending on the sign of Dirac mass [67,68]. As a result, the Chern number for the whole surface bands is  $C_x = C_x^\gamma + C_x^z$ , in which

$$\begin{aligned} C_x^\gamma &= (\text{sgn}[\Delta_x^\gamma + V_x] - \text{sgn}[\Delta_x^\gamma - V_x])/2, \\ C_x^z &= (\text{sgn}[\Delta_x^z - V_x] - \text{sgn}[\Delta_x^z + V_x])/2. \end{aligned} \quad (11)$$

It can be verified that under the condition  $\{|\Delta_x^\gamma|, |\Delta_x^z|\}_{\min} < V_x < \{|\Delta_x^\gamma|, |\Delta_x^z|\}_{\max}$ , surface Chern number  $C_x$  is 1 or  $-1$  and it can be expressed as

$$C_x = \text{sgn}[V_x] \text{sgn}[|\Delta_x^z| - |\Delta_x^\gamma|]. \quad (12)$$

Otherwise, it takes the value 0. Thus, the (100) surface behaves as a chiral TSC under appropriate parameter condition. Similarly, the surface chiral TSC will be manifested by the presence of CMHMs for the 3D system.

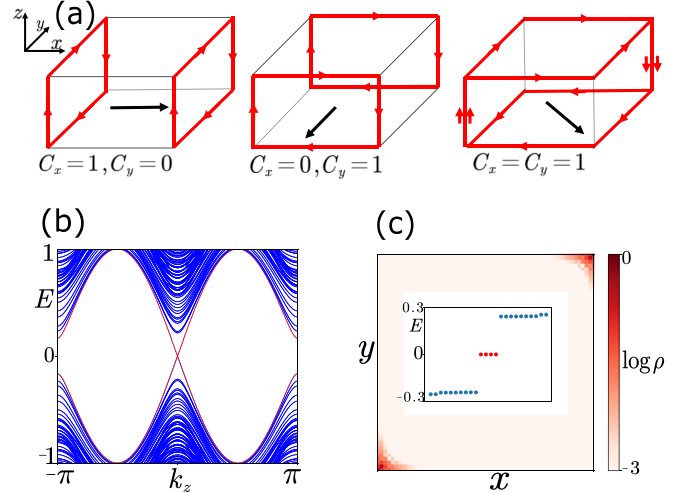


FIG. 3. (a) The distributions of the CMHMs are schematically plotted under the parameters, yielding different topological invariants  $C_x$  and  $C_y$ . The black arrow indicates the direction of in-plane magnetic field. It is noted that the CMHMs on opposite surface have identical chirality. (b) The energy spectrum of a wire geometry along  $z$  is plotted under the parameters  $m = 2$ ,  $t_x = t_y = 2$ ,  $t_z = 1$ ,  $\Delta_0 = -0.1$ ,  $\Delta_1 = 0.4$ ,  $V_x = -V_y = 0.3$ , which correspond to the topological invariants  $v_x = v_y = 0$ ,  $C_x = C_y = 1$ . The numerical calculation is performed with the size  $20 \times 20$  of the plane with open boundary condition. (c) The spatial profile of the MCMs when  $k_z = 0$  in (b) is plotted and the inset plots the energies close to zero. The numerical calculation is performed with the size  $60 \times 60$  of the plane with open boundary condition. The color bar represents the log value of the density  $\rho$  of the Majorana corner states.

When applying magnetic field along the  $y$  direction with magnitude  $V_y$ , the (010) surface has identical physics as that on the (100) surface. Under the parameter condition  $\{|\Delta_x^\gamma|, |\Delta_x^z|\}_{\min} < V_y < \{|\Delta_y^\gamma|, |\Delta_y^z|\}_{\max}$ , the surface Chern number  $C_y$  can be written as [66]

$$C_y = -\text{sgn}[V_y] \text{sgn}[|\Delta_y^z| - |\Delta_y^\gamma|]. \quad (13)$$

As we can see in Eqs. (12) and (13), the chirality of the surface chiral TSC can be tuned by reversing the direction of the magnetic field.

Consequently, the side faces can be independently tuned to a surface TSC in DIII or D symmetry class by considering the interplay between magnetic fields and superconductors. These surface TSCs are characterized by surface topological invariants  $\{v_x, v_y, C_x, C_y\}$ . In the absence of magnetic fields,  $C_x = C_y = 0$  and only HMHMs can appear at certain hinges. In the presence of magnetic fields and under the condition  $v_x = v_y = 0$ , only CMHMs can appear at certain hinges. In this case, we provide the schematic plot of the CMHMs characterized by topological invariants  $(C_x, C_y)$  in Fig. 3(a). Particularly, when  $C_x = C_y = 1$ , both (100) and (010) surfaces are chiral TSCs. There are two copies CMHMs at the hinges shared by adjacent side faces. These CMHMs will couple with each other when they have opposite chirality. On the contrary, the CMHMs with the same chirality will survive, resulting in two-channel CMHMs at certain hinges. This case can be verified by the numerical calculations, as shown in Figs. 3(b)

and 3(c). Flowing into the boundaries of the (001) surface, the two-channel CMHMs split along different directions and then converge, which forms a novel interference loop if additional magnetic flux along the  $z$  direction is applied. A topologically equivalent interference loop was obtained through the theoretical design of complicated TI-magnet-superconductor heterostructures in previous studies [13,14], and it could be used to detect the Majorana modes through the conductance interference measurement. Remarkably, relying on our proposal of achieving higher-order superconductivity based on weak topological insulators, the formation of this interference loop naturally arises from uniform 3D bulk states without complex heterostructures. Because the edge states in 2D propagate along clockwise or anticlockwise direction invariably which cannot form this interference loop, it provides an exceptional property of the second-order TSC of 3D system. Therefore, this pattern of the CMHMs not only provides the decisive evidence of the higher-order TSC, but also have great advantage in realizing quantum interference device [69,70]. The latter deserves further detailed study and we will leave it for a future study. It is also worthwhile to emphasize that the HMHMs and CMHMs can coexist in our system when the adjacent side faces behave as TRITSC and chiral TSC, respectively [66].

### III. THIRD-ORDER TSC

Similar to that second-order TSCs can be realized by performing surface TSCs, a third-order TSC with MCMs can emerge from a one-dimensional (1D) hinge TSC. In the following, we theoretically design a model of third-order TSC in D symmetry class to perform this visualized principle and provide topological characterizations for this higher-order phase.

Our model of third-order TSC is realized based on the phase for  $H_{\text{BdG}}(\mathbf{k})$  with model parameters, in which  $v_x = v_y = 0$ , but  $\Delta_x^\gamma \Delta_y^\gamma < 0$  and  $\Delta_x^z \Delta_y^z < 0$ . In this case, although both (100) and (010) surfaces are topologically trivial, the sign reversal of the pairing gaps between adjacent side faces will lead to HMHMs, which can be understood from the topological domain wall problem [71]. It is noted that because the pairing gaps of Dirac cones have sign reversal at  $k_z = 0$  and  $\pi$  simultaneously, the surface domain walls bind the hinges shared by (100) and (010) surfaces with two pairs of HMHMs. As shown in Fig. 4(a), two pairs of HMHMs cross at  $k_z = 0$  and  $\pi$ , respectively.

Based on this phase, we theoretically consider the pairing term  $\tilde{\Delta}(k_z) = (\Delta_2 + \Delta_3 \cos k_z)\tau_x s_y$ , breaking time-reversal symmetry, to gap the two pairs of HMHMs. The hinge gap can be obtained by projecting  $\tilde{\Delta}(k_z)$  into the subspace of the HMHMs. Notably, at  $k_z = 0, \pi$ , this pairing term is momentum independent. Thus, the HMHMs crossing at  $k_z = 0$  and  $\pi$  are gapped with the magnitude  $\Delta_2 + \Delta_3$  and  $\Delta_2 - \Delta_3$ , respectively. Now, we study the topology of the hinges shared by the (100) and (010) surfaces. These hinges belong to D symmetry class and have a  $Z_2$  topological classification [63–65]. The topological invariant is explicitly expressed as [72]

$$(-1)^{v_z} = \text{sgn}\left[\frac{\text{Pf}(H_{\text{hinge}}(k_z = 0))}{\text{Pf}(H_{\text{hinge}}(k_z = \pi))}\right], \quad (14)$$

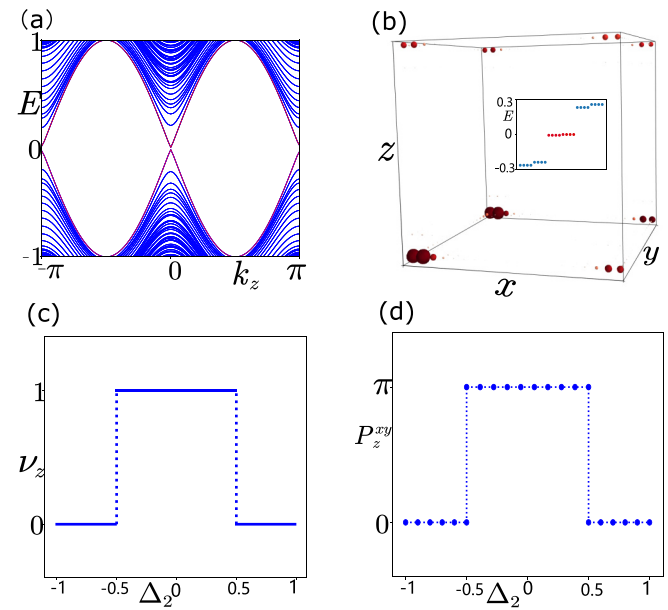


FIG. 4. (a) The energy spectrum of a wire geometry along  $z$  under the parameters  $m = 2$ ,  $t_x = 2.5$ ,  $t_y = 1$ ,  $t_z = 0.3$ ,  $\Delta_0 = -\Delta_1 = -0.5$ . The numerical calculation is performed with the size  $20 \times 20$  of the plane with open boundary condition. (b) The spatial distribution of the eight MCMs, which are obtained by considering the mass term  $0.5 \cos k_x \tau_x s_y$  to gap the HMHMs in (a). The inset shows energies close to zero. The numerical calculation is performed with the size  $20 \times 20 \times 20$  of the 3D system with open boundary condition. (c) The topological invariant  $\nu_z$  is the function of  $\Delta_2$ . (d) The numerical calculation of the nested polarization  $P_z^{xy}$ , as a function of  $\Delta_2$ .

where Pf is the Pfaffian of a antisymmetric matrix and  $H_{\text{hinge}}$  denotes the hinge Hamiltonian written in Majorana basis. The  $Z_2$  topological invariant  $\nu_z$  is 1 for the nontrivial phase and 0 for the trivial phase. At  $k_z = 0, \pi$ , the sign of Pfaffian is completely determined by the sign of the energy gap [72,73]. Consequently, the definition of  $\nu_z$  transforms into the form  $(-1)^{\nu_z} = \text{sgn}[(\Delta_2 + \Delta_3)(\Delta_2 - \Delta_3)]$ , which takes the value 0 when  $|\Delta_2/\Delta_3| > 1$  and the value 1 when  $|\Delta_2/\Delta_3| < 1$ . From the phase  $|\Delta_2| > |\Delta_3|$  to the phase  $|\Delta_2| < |\Delta_3|$ , the hinge energy gap is closed, indicating a hinge topological phase transition. Thus, the hinges are 1D TSC in D symmetry class under appropriate parameter conditions. Correspondingly, these 1D hinge TSCs will be manifested by the presence of MCMs when taking open boundary conditions of all directions. As shown in Fig. 4(b), there is one MCM located at each corner in real space. The presence of MCMs shows that the whole system is a third-order TSC.

Aside from the Pfaffian formula characterization, the hinge topology can also be revealed by the well-known nested Wilson loop topological invariants based on the equivalent topology between Wannier band and boundaries [18,19]. Performing the Wilson loop along  $k_x$  and then performing the nested Wilson loop along  $k_y, k_z$  in sequence, we obtain the nested Wilson loop polarization  $P_z^{xy}$  [18,19,66]. This topological index is quantized to  $\pi$  for the third-order TSC phase and 0 for the trivial phase. The numerical result is shown in Fig. 4(d), which exhibits a sharp topological phase transition

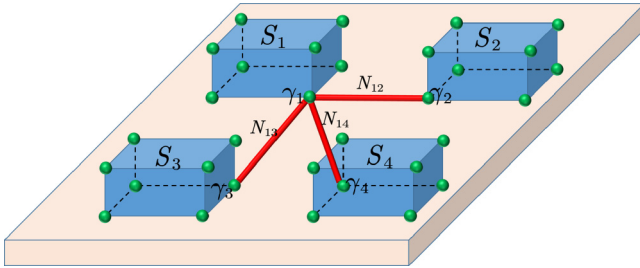


FIG. 5. The schematic diagram of the distorted Y junction formed by the third-order TSC in D class. The blue islands \$S\_{1,2,3,4}\$ denote the third-order TSC obtained through our model. The red stick denotes the nanowire. The MCMs \$\gamma\_{1,2,3,4}\$ form the distorted Y junction, in which the coupling between \$\gamma\_1\$ and \$\gamma\_{2,3,4}\$ can be tuned by the gate \$N\_{12}, N\_{13}, N\_{14}\$.

agreeing with the Pfaffian characterization shown in Fig. 4(c). Therefore, the nested polarization \$P\_z^{xy}\$ can also characterize this third-order TSC as a \$Z\_2\$ topological invariant.

Recently, the non-Abelian braiding statistics property of the MCMs have been studied in the time-reversal symmetry-breaking second-order TSC through locally tuning the topological phase transition [51,52] or MCMs coupling [46] by electronic gating. For our third-order TSC in D symmetry class, the former proposal is hard to achieve because the bulk is 3D. Meanwhile, the latter proposal only needs to control the coupling between MCMs and can be applied. In our model, each of four third-order TSCs can provide one MCM to form the distorted Y junction [74,75], as shown in Fig. 5. The four MCMs \$\gamma\_{1,2,3,4}\$ originating from different TSC islands are connected by 1D nanowires (red lines in Fig. 5). The coupling between the MCMs \$\gamma\_1\$ and \$\gamma\_j\$ (\$j = 2, 3, 4\$) can be tuned by gating the nanowires. Then the MCMs \$\gamma\_3\$ and \$\gamma\_4\$ can be exchanged by coupling the MZMs \$\{\gamma\_1, \gamma\_2\}, \{\gamma\_1, \gamma\_3\}, \{\gamma\_1, \gamma\_4\}, \{\gamma\_1, \gamma\_2\}\$ in sequence [74,75].

#### IV. DISCUSSION AND CONCLUSION

Weak TIs, as the stacking of 2D strong TI, have been confirmed in some real materials (e.g., Bi<sub>4</sub>I<sub>4</sub> [76], ZrTe<sub>5</sub> [77,78], HfTe<sub>5</sub> [79]). It is also shown that some real materials, such as TaSe<sub>3</sub> [80], CaSn [81], CaBi<sub>2</sub> [82], WTe<sub>2</sub>(MoTe<sub>2</sub>) [83], can display the combination of the superconductivity and the weak TI phase, which provides a platform to explore intrinsic TSCs based on weak TIs rather than strong TI. Particularly, it is theoretically predicted that iron-based superconductors Li(OH)FeSe [55] and CaFeAs<sub>2</sub> [84] are 3D weak TI characterized by the \$Z\_2\$ topological invariants (0;001) [4]. And the HMHMs generated by the interplay between the bulk \$s\_\pm\$-wave pairing and topological surface states in iron-based SC FeTe<sub>1-x</sub>Se<sub>x</sub> [43] have been supported from the experimental evidence [85]. Thus, our models can reasonably capture the topology property of iron-based SC Li(OH)FeSe and CaFeAs<sub>2</sub>. On the other hand, the HMHMs in our model can be generated as long as the superconducting pairing gap the two surface Dirac cones with opposite sign, which can also be introduced by the superconducting proximity effect on the side face of the weak TI.

For simplicity, we have taken the chemical potential to be zero in our discussion. However, our conclusions do not depend on this condition. The Majorana hinge modes and MCMs can survive in the presence of finite chemical potential as long as the bulk and boundary gaps preserve. Similarly, these boundary states are robust against the perturbations preserving bulk and boundary gaps, even though they couple the two Dirac cones on the same side face.

In our models, the higher-order topology originates from the boundary (surface or hinge) TSCs essentially. Actually, the principle that constructing the boundary TIs or TSCs to realize the higher-order TIs or TSCs is general and weak TI is a good platform to perform this principle. It is known that weak TI features an even number of surface states on certain surfaces. On the other hand, it is shown that gapped boundary states of weak TIs allow topologically nontrivial classification for the surface [86,87], which enables the weak TIs to become a good platform to perform the boundary TI or TSC when considering additional mass term. Thus, an odd number of the surface Dirac cones with negative energy gap are topologically distinguished from an even number of the surface Dirac cones with negative energy gap. The former case corresponds to the realization of boundary TI or TSC, which enables the whole system to display the higher-order topology.

In conclusion, based on the weak TIs with band inversion at both \$\Gamma\$ and \$Z\$ points, we consider the interplay between superconductors and magnetic fields in this system to realize second-order TSCs featuring HMHMs or CMHMs and third-order TSC featuring MCMs. The chiral Majorana hinge modes and MCMs in our models originate from the surface and hinge TSC, respectively. Correspondingly, these higher-order TSCs can be characterized by corresponding boundary topological invariants. Particularly, the CMHMs in our proposal can naturally form a quantum interference loop, which not only can be used in detecting the second-order TSC, but also pave the way to implementation of the Majorana quantum interference device from the higher-order TSCs.

#### ACKNOWLEDGMENTS

We would like to thank C.-X. Liu and X.-J. Liu for useful discussions. This work is supported by NSFC (Grant No. 12074133), NSFC (Grant No. 11674114), and National Key R&D Program of China (Grant No. 2016YFA0401003).

#### APPENDIX A: TOPOLOGY OF THE (010) SURFACE

In this Appendix, we focus on the topology of the (010) surface. To obtain the surface Hamiltonian, we take the open boundary condition of the \$y\$ direction. Under this condition, we replace \$k\_y \rightarrow -i\partial\_y\$, then the BDG Hamiltonian expanding at \$\Gamma\$ and \$Z\$ points can be decomposed as \$H\_{\text{BDG}}^{\gamma(z)} = H\_0^{\gamma,z}(y) + H\_p^{\gamma(z)}(y, k\_x, k\_z)\$, in which

$$H_0^{\gamma(z)}(y) = \left( m_{\gamma(z)} - \frac{t_y}{2} \partial_y^2 \right) \tau_z \sigma_z - i\partial_y \tau_z \sigma_x s_y,$$

$$H_p^{\gamma(z)}(y, k_x, k_z) = k_x \sigma_x s_x \pm k_z \sigma_x s_z + \Delta(y) \tau_y s_y, \quad (\text{A1})$$

where \$\Delta(y)\$ is defined as \$\bar{\Delta} + \frac{\Delta\_1 \partial\_y^2}{2}\$ and the insignificant terms \$k\_x^2\$ and \$k\_z^2\$ involved have been omitted. Now we solve the zero-

energy states of  $H_0^{\gamma(z)}$  and consider  $H_p^{\gamma(z)}$  as a perturbation to extract the surface Hamiltonian.

Solving the eigenequation  $H_p^{\gamma(z)}|\psi_\alpha^{\gamma(z)}(y)\rangle=0$  under the boundary conditions  $|\psi_\alpha^{\gamma(z)}(y=0)\rangle=|\psi_\alpha^{\gamma(z)}(y=-\infty)\rangle=0$ , there are four zero-energy states. The wave function of these zero states can be written as

$$|\psi_\alpha^{\gamma(z)}(y)\rangle=\mathcal{N}_{\gamma,z}\sin(\kappa_1^{\gamma(z)}y)e^{\kappa_2 y}|\xi_\alpha\rangle, \quad (\text{A2})$$

with  $\kappa_1^{\gamma(z)}=\sqrt{2|m_{\gamma(z)}|/t_y-1/t_y^2}$ ,  $\kappa_2=1/t_y$ , and  $\mathcal{N}_{\gamma,z}$  the normalization factors. Spinor  $|\xi_\alpha\rangle$  satisfies  $\sigma_y s_y |\xi_\alpha\rangle=|\xi_\alpha\rangle$ . We choose them as

$$\begin{aligned} |\xi_1\rangle &= |\tau_y=+1\rangle\otimes|\sigma_y=+1\rangle\otimes|s_y=+1\rangle, \\ |\xi_2\rangle &= |\tau_y=-1\rangle\otimes|\sigma_y=-1\rangle\otimes|s_y=-1\rangle, \\ |\xi_3\rangle &= |\tau_y=+1\rangle\otimes|\sigma_y=-1\rangle\otimes|s_y=-1\rangle, \\ |\xi_4\rangle &= |\tau_y=-1\rangle\otimes|\sigma_y=+1\rangle\otimes|s_y=+1\rangle. \end{aligned} \quad (\text{A3})$$

Projecting  $H_p$  into the subspace spanned by these four zero-energy states, the low-energy surface Hamiltonian can be written as

$$\tilde{H}^{\gamma(z)}=-k_x\tilde{\tau}_x\tilde{s}_0\pm k_z\tilde{\tau}_y\tilde{s}_z+\Delta_y^{\gamma,z}\tilde{\tau}_z\tilde{s}_0, \quad (\text{A4})$$

where  $\Delta_y^{\gamma(z)}=\bar{\Delta}+2\Delta_1 m_{\gamma(z)}/t_y$  denote the superconducting pairing gap of the Dirac cones, Pauli matrices  $\tilde{\tau}$  and  $\tilde{s}$  act in the zero-energy states space. When  $\Delta_y^{\gamma}\Delta_y^z<0$ , the (010) surface exists an odd number of Fermi surfaces with negative superconducting pairing. In this case, the (010) surface behaves as a TRITSC. As a result, the topology of the (010) surface can be characterized by the surface  $Z_2$  topological invariant

$$(-1)^{\nu_y}=\text{sgn}(\Delta_y^{\gamma}\Delta_y^z). \quad (\text{A5})$$

The condition  $\nu_y=1$  indicates the realization of surface TRITSC and it leads to

$$-2+|m_z|/t_y<\Delta_0/\Delta_1<-2+|m_y|/t_y. \quad (\text{A6})$$

Further considering the Zeeman term  $V_y s_y$  induced by the magnetic field along the  $y$  direction, then the surface Hamiltonian in Eq. (A4) transforms into the form

$$\tilde{H}^{\gamma(z)}=-k_x\tilde{\tau}_x\tilde{s}_0\pm k_z\tilde{\tau}_y\tilde{s}_z+\Delta_y^{\gamma(z)}\tilde{\tau}_z\tilde{s}_0+V_y\tilde{\tau}_z\tilde{s}_z. \quad (\text{A7})$$

Obviously, the obtained surface Hamiltonian is block diagonal and each block contributes half Chern number. Therefore, the Chern number for the whole surface bands is  $C_y=C_y^{\gamma}+C_y^z$ , in which

$$\begin{aligned} C_y^{\gamma} &= (\text{sgn}[\Delta_y^{\gamma}-V_y]-\text{sgn}[\Delta_y^{\gamma}+V_y])/2, \\ C_y^z &= (\text{sgn}[\Delta_y^z+V_y]-\text{sgn}[\Delta_y^z-V_y])/2. \end{aligned} \quad (\text{A8})$$

Under the condition  $\{|\Delta_y^{\gamma}|, |\Delta_y^z|\}_{\min}< V_y < \{|\Delta_y^{\gamma}|, |\Delta_y^z|\}_{\max}$ ,  $C_y$  takes value 1 or -1 and it can be expressed as

$$C_y=-\text{sgn}[V_y]\text{sgn}[|\Delta_y^{\gamma}|-|\Delta_y^z|]. \quad (\text{A9})$$

Otherwise, it takes the value 0.

## APPENDIX B: COMPARISON WITH THE HMHMS PHASE BASED ON STRONG TI AND TRIVIAL INSULATOR

It is noted that when considering the bulk  $s_{\pm}$  pairing, the strong TI phase [43] and trivial insulator phase [54] can also

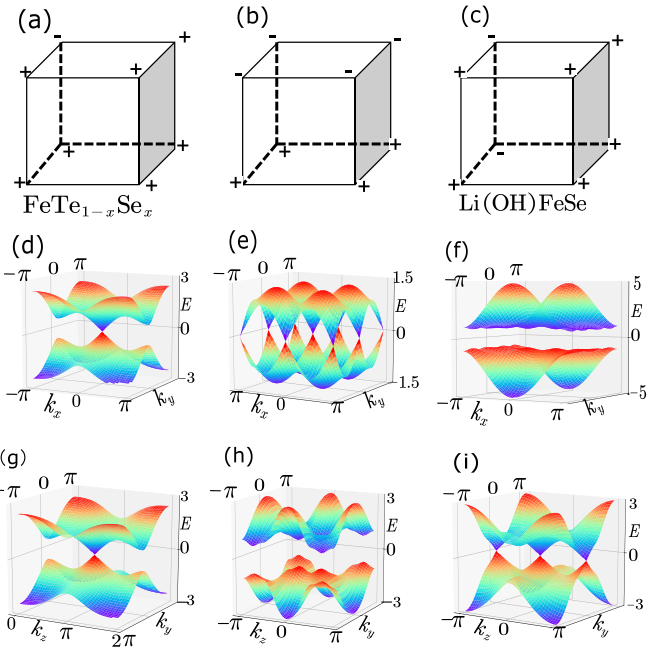


FIG. 6. (a)–(c) At TRI momentum points, the parity distributions of the strong TI phase in  $\text{FeTe}_{1-x}\text{Se}_x$ , trivial insulator, and weak TI phase in  $\text{Li}(\text{OH})\text{FeSe}$ , respectively. The +, - represent the eigenvalues of the inversion operator. (d)–(f) The energy spectrum of the (001) surface in the strong TI, trivial insulator, and weak TI phases. (g)–(i) The energy spectrum of the (100) surface in the strong TI, trivial insulator, and weak TI phases. In our numerical calculations, model parameters are taken as  $m_0=2$ ,  $t_x=1$ ,  $t_y=1$ ,  $t_z=-0.5$  in the strong TI phase. Model parameters are taken as  $m_0=0$ ,  $t_x=-1$ ,  $t_y=-1$ ,  $t_z=3$  in the trivial insulator phase. Model parameters are taken as  $m_0=2$ ,  $t_x=2$ ,  $t_y=2$ ,  $t_z=1$  in the weak TI phase.

display the HMHMs on the (001) surface. Here, we compare the mechanism of realizing the HMHMs phase between our work and the other two works. It is noted that these three higher-order models can be uniformly described by the BDG Hamiltonian  $H_{\text{BDG}}(\mathbf{k})$  when taking different model parameters. For the HMHMs phase based on strong TI, the normal state has band inversion at the  $Z$  points, which can be described by the four  $Z_2$  topological invariants (1; 000). For the HMHMs phase based on trivial insulator, the normal state has band inversion at the  $k_z=\pi$  plane, which can be described by the four  $Z_2$  topological invariants (0; 000). However, the HMHMs phase we considered is based on a weak TI and the normal state has the band inversion at both  $\Gamma$  and  $Z$  points, which can be described by the four  $Z_2$  topological invariants (0; 001). The band inversion configurations of these three cases are shown in Figs. 6(a)–6(c).

Owing to the different band-inversion configurations, these three different phases of normal state have different surface states. For the strong TI, every surface has one surface Dirac cone, as shown in Figs. 6(d) and 6(g). For the trivial insulator with the band inversion at  $k_z=\pi$ , the (001) surface of this system has four surface Dirac cones and the side faces are fully gapped, as shown in Figs. 6(e) and 6(h), respectively. For the weak TI we considered, every side face has two Dirac cones and the (001) surface is fully gapped, as shown in

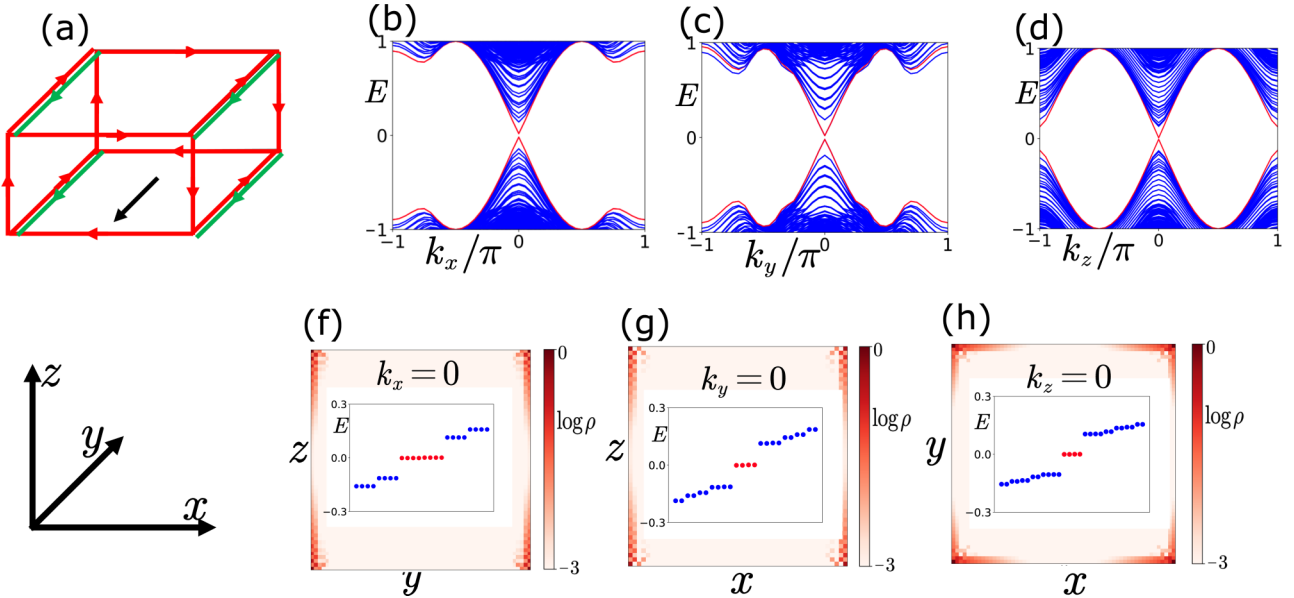


FIG. 7. Common parameters are taken as  $m = 2$ ,  $t_x = t_y = 2$ ,  $t_z = 1$ ,  $\Delta_0 = -0.3$ ,  $\Delta_1 = 0.4$ ,  $V_y = 0.2$ . These parameters yield surface topological invariants  $v_x = 1$ ,  $v_y = 0$ ,  $C_x = 0$ ,  $C_y = 1$ . (a) Schematic plot of the distribution of CHHMMs and HHMMs. (b)–(d) The energy spectrum of a wire geometry along  $x$ ,  $y$ ,  $z$  directions, respectively. The numerical calculation is performed with the size  $20 \times 20$  of the plane with open boundary condition. (e)–(g) The spatial profile of the CMZMs when  $k_x = 0$ ,  $k_y = 0$ ,  $k_z = 0$  in (b)–(d) and the insets plot the energies close to zero. The numerical calculation is performed with the size  $60 \times 60$  of the plane with open boundary condition. The color bar represents the log value of the density  $\rho$  of the Majorana corner states.

Figs. 6(f) and 6(i), respectively. With the different surface states, the mechanism of realizing the HMHMs phase when considering the bulk  $s_{\pm}$  pairing is different. For the HMHMs phase based on strong TI, the HMHMs can be attributed to the formation of the surface domain wall between (001) surface and side surfaces [43]. For the HMHMs based on trivial insulators, the four surface Dirac cones are gapped with a nontrivial way, which enables the (001) surface to behave as a TRITSC [54]. In our model, this HMHMs phase attributed the nontrivial topology of the (100) and (010) surfaces as elucidated in the main text.

### APPENDIX C: COEXISTENCE OF HHMMs AND CHHMMs

In this Appendix, we show that the HHMMs and CHHMMs can coexist in our system. This scenario can be achieved when the adjacent side faces behave as TRITSC and chiral TSC, respectively. For example, applying finite magnetic field along the  $y$  direction to the second-order TSC characterized by topological invariants  $v_x = 1$ ,  $v_y = 0$ , then the (010) surface is driven to a chiral TSC. In this case, we obtain second-order TSC characterized by topological invariants  $v_x = 1$ ,  $v_y = 0$ ,  $C_x = 0$ ,  $C_y = 1$ . As schematically plotted in Fig. 7(a), HHMMs and CHHMMs can coexist in this system. In Figs. 7(b)–7(g), we check the distribution of the HHMMs and CHHMMs in Fig. 7(a) through numerical calculations.

### APPENDIX D: OTHER HIGHER-ORDER TI OR TSC MODELS BASED ON WEAK TI

In our higher-order models, we start from one type typical weak TI with band inversion at both  $\Gamma$  and  $Z$  points. For this phase, as long as the considered mass term can gap the two

Dirac cones localized at the side face with opposite sign, the higher-order TI or TSC can be realized. This principle is also suitable in the 2D case and it can be best exemplified by the well-known Benalcazar-Bernevig-Hughes (BBH) model [18].

The BBH model is a typical second-order TI, which has been widely studied. Here, we provide a perspective about the BBH model that it can be recast through gapping the edge states of the weak TI with opposite sign. The bulk Hamiltonian of the BBH model can be separated as

$$\begin{aligned} H_{\text{BBH}} &= H_{\text{WTI}} + (\gamma_y + \lambda_y \cos k_y) \Gamma_4, \\ H_{\text{WTI}} &= (\gamma_x + \lambda_x \cos k_x) \Gamma_1 + \lambda_x \sin k_x \Gamma_2 + \lambda_y \sin k_y \Gamma_3, \\ \Gamma_1 &= \tau_x \sigma_0, \quad \Gamma_2 = -\tau_y \sigma_z, \quad \Gamma_3 = -\tau_y \sigma_x, \quad \Gamma_4 = -\tau_y \sigma_y, \end{aligned} \quad (\text{D1})$$

with  $\tau$  and  $\sigma$  two set Pauli matrices. When  $|t_x| < |\lambda_x|$ , the Hamiltonian  $H_{\text{WTI}}$  behaves as the weak TI with the band inversion at two TRI momenta of the  $k_x = 0$  or  $\pi$ . There are two pairs of helical edge states along the  $x$  edge and the  $y$  edge is fully gapped, as shown in Figs. 8(a) and 8(b). Based on this 2D weak TI, the additional mass term  $(\gamma_y + \lambda_y \cos k_y) \Gamma_4$  gaps the two pairs of helical states with opposite sign when  $|t_y| < |\lambda_y|$ , as shown in Fig. 8(c). Thus, when  $|\gamma_{x,y}| < |\lambda_{x,y}|$ , the  $x$  edge behaves as a 1D TI and there are the corner states. It is noted that the mass term  $(\gamma_y + \lambda_y \cos k_y) \tau_x \sigma_x$  can also gap the two pairs of edge states of  $H_{\text{WTI}}$  with opposite sign when  $|\gamma_y| < |\lambda_y|$ , as shown in Fig. 8(d). This model is also a second-order TI when both the bulk and edge are gapped.

In the main text, we design the higher-order TSC based on the 3D weak TI characterized by the four  $Z_2$  topological invariants (0;001). However, the different band inversion at the eight TRI momenta in 3D can generate different types of

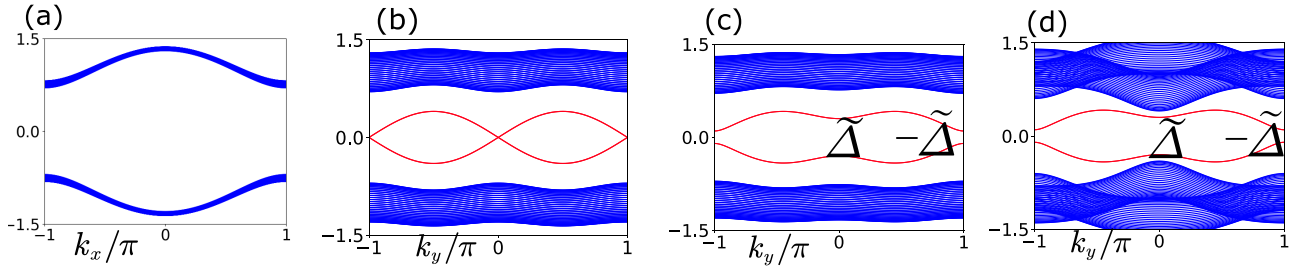


FIG. 8. The model parameters are taken as  $\lambda_x = 1$ ,  $\gamma_x = 0.3$ ,  $\gamma_y = 0.1$ ,  $\lambda_y = 0.2$ . (a), (b) The energy spectrums of a wire geometry of the Hamiltonian  $H_{\text{WTI}}$  along the  $x$  and  $y$  directions, respectively. (c), (d) The two pairs of edge states in (b) are gapped by the mass terms  $(\gamma_y + \lambda_y)\Gamma_4$  and  $(\gamma_y + \lambda_y)\tau_x\sigma_x$ , respectively.  $\tilde{\Delta}$  and  $-\tilde{\Delta}$  denote the opposite energy gap for the two pairs of helical edge states. These numerical calculations are performed with the size 30 of the open boundary condition along the  $x$  direction.

weak TIs. For example, considering the 3D weak TI described by the Hamiltonian

$$H = \left(1/2 - \sum_{i=x,y,z} \cos k_i\right) \sigma_z s_0 + \sum_{i=x,y,z} \sin k_i \sigma_x s_i, \quad (\text{D2})$$

which has the band inversion at the TRI momenta points  $(0, 0, 0)$ ,  $(0, \pi, 0)$ ,  $(\pi, 0, 0)$ ,  $(0, 0, \pi)$ . Then this weak TI is characterized by the four  $Z_2$  topological invariants  $(0;111)$  and there are two surface Dirac cones on the  $(100)$ ,  $(010)$ , and  $(001)$  surfaces, as shown in Figs. 9(a)–9(c). Further considering the bulk  $s_{\pm}$  pairing  $\Delta(\mathbf{k}) = \Delta_0 + \Delta_1(\cos k_x + \cos k_y)$ , the two Dirac cones on the  $(100)$  surface are gapped with the magnitude  $\Delta_0 + \frac{3\Delta_1}{2}$  and  $\Delta_0 - \frac{\Delta_1}{2}$ . Due to the fourfold rotation symmetry, the two Dirac cones of the  $(010)$  surface are gapped with the same magnitudes as the Dirac cones of the  $(100)$  surface. The two Dirac cones of the  $(001)$  surface are gapped with the same magnitude  $\Delta$ . Thus, when  $\frac{1}{2} < |\Delta_0/\Delta_1| < \frac{3}{2}$ , the two Dirac cones of the  $(100)$  and  $(010)$  surfaces are gapped with opposite sign, which enables the realization the surface

TSC and there are HMHMs at the hinges shared between the  $(001)$  surface and other surfaces, as shown in Figs. 9(d)–9(f).

## APPENDIX E: WILSON LOOP AND NESTED WILSON LOOP

### 1. Wilson loop

In this Appendix, we introduce the standard procedure of calculating the Wilson loop and the nested Wilson loop [18,19], which can characterize the HMHMs and MCMs, respectively. Considering the Wilson loop along  $k_x$ , the Wannier center can be obtained by diagonalizing the Wilson loop matrix

$$W_{x,k}|v_{x,k}^j\rangle = \exp[i p_x^j(k_y, k_z)]|v_{x,k}^j\rangle. \quad (\text{E1})$$

Here,  $j \in \{1, \dots, N_{\text{occ}}\}$  with  $N_{\text{occ}}$  the number of occupied states,  $W_{x,k}$  is  $N_{\text{occ}} \times N_{\text{occ}}$  matrix with matrix element  $W_{x,k}^{nm} = \lim_{N_x \rightarrow \infty} \langle n, \mathbf{k} + \mathbf{G}_x | [\prod_{s=1}^{N_x-1} P_x(\mathbf{k}_s)] | m, \mathbf{k} \rangle$ , where  $|m, \mathbf{k}\rangle$  is the  $m$ th occupied state at  $\mathbf{k}$ , and  $\mathbf{G}_x$  denotes reciprocal vector along the  $x$  direction, the projector operator  $P_x(\mathbf{k}_s)$  for the

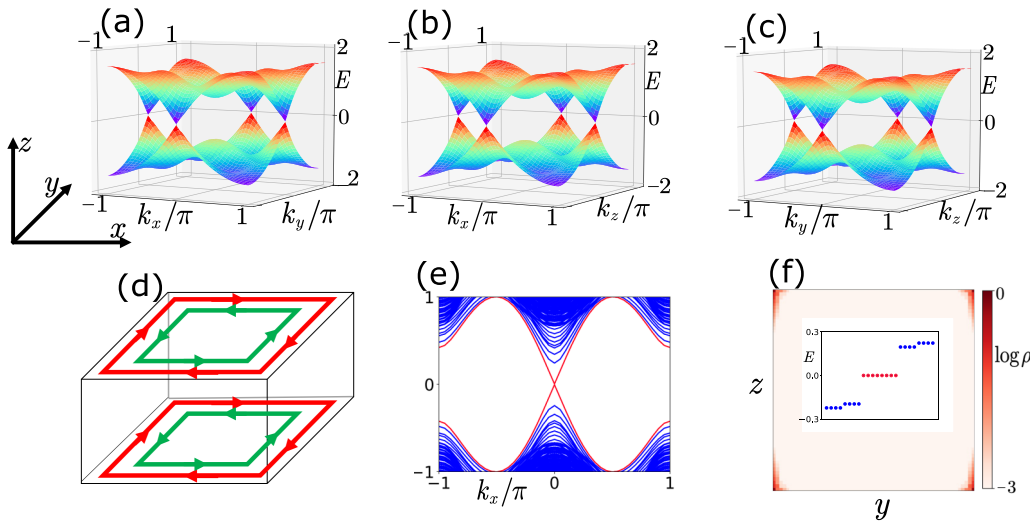


FIG. 9. The model parameters are taken as  $\Delta_0 = -\Delta_1 = 0.4$ . (a)–(c) The energy spectrum of the surface states of the WTI characterized by the four  $Z_2$  topological invariants  $(0;111)$ . (d) The distributions of the HMHMs are schematically plotted. (e) The energy spectrums of a wire geometry along the  $x$  directions. The numerical calculations are performed with the size  $20 \times 20$  of the  $y$ - $z$  plane with open boundary condition. (f) The spatial profile of the MCMs when  $k_x = 0$  in (e), with the size  $60 \times 60$  of the  $y$ - $z$  plane. The color bar represents the log value of the density  $\rho$  of the Majorana corner states.

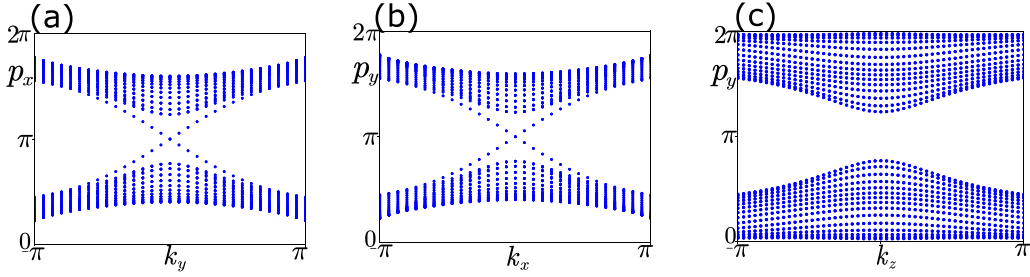


FIG. 10. Common parameters are taken as  $m = 2$ ,  $t_x = t_y = 2$ ,  $t_z = 1$ ,  $\Delta_0 = -0.5$ ,  $\Delta_1 = 0.5$ . These parameters yield surface topological invariants  $v_x = v_y = 1$ . (a) The Wannier spectrum  $p_x(k_y)$  is plotted by performing the Wilson loop along  $k_x$  for the slab geometry on the (001) surface. (b) The Wannier spectrum  $p_y(k_x)$  is plotted by performing the Wilson loop along  $k_y$  for the slab geometry on the (001) surface. (c) The Wannier spectrum  $p_y(k_z)$  is plotted by performing the Wilson loop along  $k_y$  for the slab geometry on the (100) surface.

occupied states is defined as  $P_x(\mathbf{k}_s) = \sum_{j=1}^{N_{\text{occ}}} |j, \mathbf{k}_s\rangle \langle j, \mathbf{k}_s|$ , with  $\mathbf{k}_s = \mathbf{k} + \frac{s}{N_s} \mathbf{G}_x$ .

The HMHMs can be characterized by the winding of the Wannier center obtained for the system with a slab geometry. For example, the second-order TSC phase characterized by topological invariants  $v_x = v_y = 1$  hosts HMHMs at the hinges shared by the (001) surface and side surfaces. To characterize these HMHMs, we consider the slab geometry on the (001) surface with the open boundary condition of the  $z$  direction. For this system, the Wannier centers  $p_x(k_y)$  and  $p_y(k_x)$  are obtained by performing Wilson loop along  $k_x$  and  $k_y$ , respectively. As shown in Figs. 10(a) and 10(b), the Wannier centers  $p_x(k_y)$  and  $p_y(k_x)$  exhibit a helical winding as the HMHMs, which signal the existence of the HMHMs. However, when considering the slab geometry on the (100) surface and performing the Wilson loop along  $k_y$ , the Wannier spectrum  $p_y(k_z)$  is gapped, as shown in Fig. 10(c).

## 2. Nested Wilson loop

To characterize the third-order TSC in the main text, we perform the Wilson loop along  $k_x$  and the nested Wilson loop along  $k_y$ ,  $k_z$  in sequence for eight-band Hamiltonian  $H_{\text{BDG}}(\mathbf{k}) + \tilde{\Delta}(k_z)$  in momentum space. Performing the Wilson loop along  $k_x$  as Eq. (E1), we obtain 2D Wannier band  $p_x(k_y, k_z)$ , which is gapped when the energy spectrum of the (100) surface is gapped. As shown in Fig. 11(a), the Wannier gap splits the

Wannier spectrum  $p_x(k_y, k_z)$  into two sectors  $p_x^{\pm}(k_y, k_z)$  associated with corresponding eigenstates  $|v_{x,k}^{\pm,r}\rangle$ , with  $r = 1, 2$ . Based on the eigenstates  $|v_{x,k}^{\pm,r}\rangle$ , we construct the nested Wannier basis

$$|w_{x,k}^{+,r}\rangle = \sum_{j=1}^4 |j, \mathbf{k}\rangle [v_{x,k}^{+,r}]^j, \quad (\text{E2})$$

where  $[v_{x,k}^{+,r}]^j$  is the  $j$  component of the eigenstate  $|v_{x,k}^{+,r}\rangle$ . Calculating the nested Wilson loop along  $k_y$ , the nested Wannier spectrum can be obtained by diagonalizing the matrix

$$\mathcal{W}_{y,k}^+ |\eta_{y,k}^+\rangle = \exp[i p_y^x(k_z)] |\eta_{y,k}^+\rangle. \quad (\text{E3})$$

Here,  $\mathcal{W}_{y,k}^+$  is  $2 \times 2$  matrix with matrix element  $(\mathcal{W}_{y,k}^+)^{rr'} = \lim_{N_y \rightarrow \infty} \langle w_{x,k+G_y}^{+,r} [\prod_{q=1}^{N_y-1} P(\mathbf{k}_q)] | w_{x,k}^{+,r'} \rangle$ , where  $\mathbf{G}_y$  denotes reciprocal vector along the  $y$  direction, the projecting operator  $P(\mathbf{k}_q)$  is defined as  $P(\mathbf{k}_q) = \sum_{r=1}^2 |w_{x,k_q}^{+,r}\rangle \langle w_{x,k_q}^{+,r}|$ , with  $\mathbf{k}_q = \mathbf{k} + \frac{q}{N_y} \mathbf{G}_y$ . The nested Wannier band  $p_y^x(k_z)$  is gapped when the energy spectrum of the hinges shared by the (100) and (010) surfaces is gapped. As shown in Fig. 11(b), the Wannier gap splits the nested Wannier spectrum  $p_y^x(k_z)$  into two sectors  $p_y^{x\pm}$  with corresponding eigenstates  $|\eta_{y,k}^{x\pm}\rangle$ . We choose Wannier sector  $p_y^{x+}$  to construct Wannier basis

$$|\tilde{w}_{y,k}^{+,+}\rangle = \sum_{r=1}^2 |w_{x,k}^{+,r}\rangle [\eta_{y,k}^{+,+}]^r, \quad (\text{E4})$$

where  $[\eta_{y,k}^{+,+}]^r$  is the  $r$  component of the eigenstate  $|\eta_{y,k}^{+,+}\rangle$ . The nested Wilson loop along  $k_z$  can be performed by diagonalizing the matrix

$$\tilde{\mathcal{W}}_{z,k}^{+,+} |\tilde{\eta}_{z,k}^{+,+}\rangle = \exp[i p_z^{xy}] |\tilde{\eta}_{z,k}^{+,+}\rangle. \quad (\text{E5})$$

Here,  $\tilde{\mathcal{W}}_{z,k}^{+,+} = \lim_{N_z \rightarrow \infty} \langle \tilde{w}_{y,k+G_z}^{+,+} [\prod_{l=1}^{N_z-1} P_z(\mathbf{k}_l)] | \tilde{w}_{y,k}^{+,+} \rangle$ , where  $\mathbf{G}_z$  denotes reciprocal vector along the  $z$  direction, the projecting operator  $P_z(\mathbf{k}_l)$  is defined as  $P_z(\mathbf{k}_l) = |\tilde{w}_{y,k_l}^{+,+}\rangle \langle \tilde{w}_{y,k_l}^{+,+}|$ , with  $\mathbf{k}_l = \mathbf{k} + \frac{l}{N_z} \mathbf{G}_z$ . Finally, we obtain nested polarization

$$P_z^{xy} = -i \frac{1}{N_x N_y} \sum_{k_x, k_y} \ln[p_z^{xy}]. \quad (\text{E6})$$

Here, it is noted that the order of the nested Wilson loops  $W_x \rightarrow \mathcal{W}_y$  is arbitrary to characterize the third TSC.

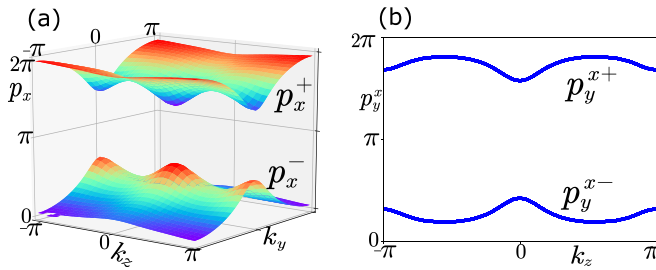


FIG. 11. The Wannier bands are obtained by calculating the Wilson loop and the nested Wilson loop based on the Hamiltonian  $H_{\text{BDG}}(\mathbf{k}) + \tilde{\Delta}(k_z)$ . The parameters are taken as  $m = 2$ ,  $t_x = 2.5$ ,  $t_y = 1$ ,  $t_z = 0.3$ ,  $\Delta_0 = -\Delta_1 = -\Delta_3 = -0.5$ ,  $\Delta_2 = 0$ . (a) 2D Wannier spectrum  $p_x(k_y, k_z)$  is plotted by performing the Wilson loop along  $k_x$ . (b) Nested Wannier spectrum  $p_y^x(k_z)$  is plotted by performing the nested Wilson loop along  $k_y$ .

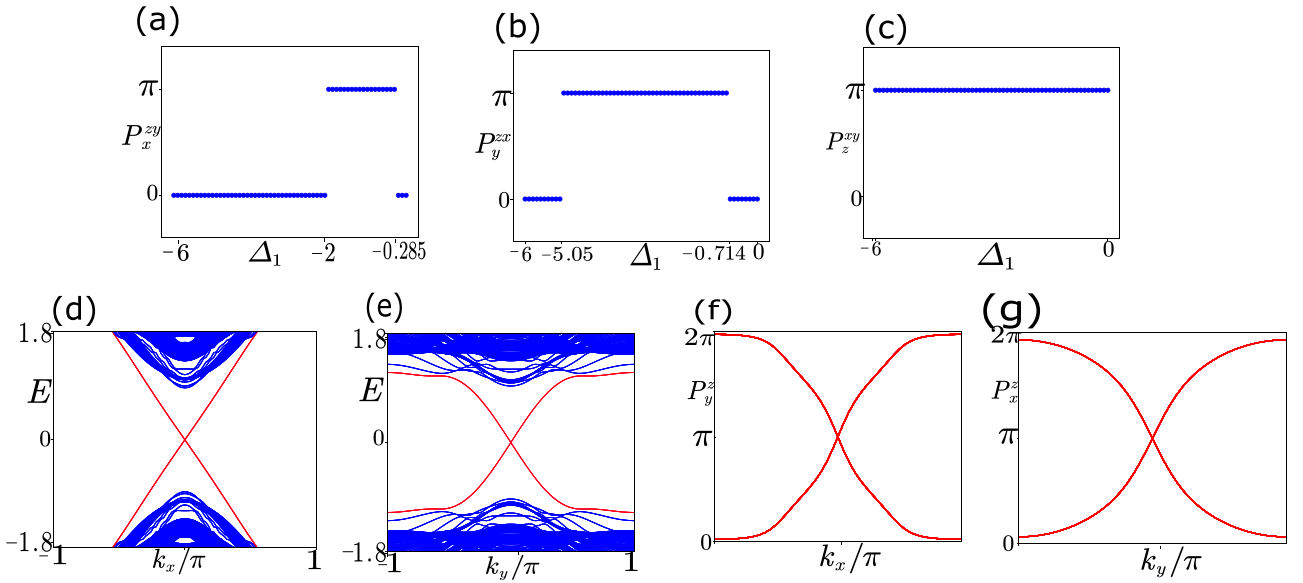


FIG. 12. Common parameters are taken as  $m = 2$ ,  $t_x = 2.5$ ,  $t_y = 1$ ,  $t_z = 0.3$ ,  $\Delta_2 = 0$ ,  $\Delta_0 = \Delta_3 = 1$ . (a)–(c) The nested polarizations  $P_x^{zy}$ ,  $P_y^{xz}$ ,  $P_z^{xy}$  is a function of  $\Delta_1$ . (d) The energy spectrum of a wire geometry along  $x$  at the phase transition point  $\Delta_1 = -2$  of  $P_x^{zy}$ . The numerical calculation is performed with the size  $20 \times 20$  of the plane with open boundary condition. (e) The energy spectrum of a wire geometry along  $y$  at the phase transition point  $\Delta_1 = -0.714$  of  $P_y^{xz}$ . The numerical calculation is performed with the size  $20 \times 20$  of the plane with open boundary condition. (f) The nested Wannier band  $P_y^z(k_x)$  at the phase transition point  $\Delta_1 = -2$  of  $P_x^{zy}$ . (g) The nested Wannier band  $P_x^z(k_y)$  at the phase transition point  $\Delta_1 = -0.714$  of  $P_y^{xz}$ .

### 3. Characterizing the hinge topological phase transition

In the main text, we have shown that the third-order TSC can be designed through the 1D hinge TSC and the MCMs can be characterized by the Pfaffian formula and the nested Wilson loop topological invariants  $P_z^{xy}$ . Actually, the MCMs in our model can exist in extensive parameter regions as long as the bulk, surface, and hinge energy gap remained. The obtained third-order TSC is characterized by the well-known nested Wilson loop topological invariants ( $P_x^{zy}$ ,  $P_y^{xz}$ ,  $P_z^{xy}$ ), similar to the topological octupole insulator model [18]. That is to say, when  $P_x^{yz} = P_y^{xz} = P_z^{xy} = \frac{1}{2}$ , the MCMs appear. Once these nested Wilson loop polarizations jump from the quantized value  $(\frac{1}{2}, \frac{1}{2}, \frac{1}{2})$  to the value  $(0, \frac{1}{2}, \frac{1}{2})$ , or  $(\frac{1}{2}, 0, \frac{1}{2})$ , or  $(0, 0, \frac{1}{2})$ , the hinge energy gap along  $k_x$ , or  $k_y$ , or  $k_z$  must be closed, indicating the hinge topological phase transition. We calculate the nested polarization  $P_z^{xy}$ ,  $P_y^{xz}$ ,  $P_x^{zy}$  with standard method to

explore the larger topological parameters regions. As shown in Figs. 12(a)–12(c), in the region  $-2 < \Delta_1 < -0.285$  and  $-5.05 < \Delta_1 < -0.714$ ,  $P_x^{zy} = P_y^{xz} = \frac{1}{2}$ , and  $P_z^{xy} = \frac{1}{2}$  in all the range. Therefore, the system is a third-order TSC with MCMs in the region  $-2 < \Delta_1 < -0.714$  when  $m = 2$ ,  $t_x = 2.5$ ,  $t_y = 1$ ,  $t_z = 0.3$ ,  $\Delta_2 = 0$ ,  $\Delta_0 = \Delta_3 = 1$ . At the phase transition point  $\Delta_1 = -2$  of  $P_x^{zy}$ , the hinge energy gap along the  $x$  direction is closed, which can be reflected by the winding of the nested Wannier band  $P_y^z(k_x)$ , as shown in Figs. 12(d) and 12(f), respectively. At the phase transition point  $\Delta_1 = -0.714$  of  $P_y^{xz}$ , the hinge energy gap along the  $y$  direction is closed, which can be reflected by the winding of the nested Wannier band  $P_x^z(k_y)$ , as shown in Figs. 12(e) and 12(g), respectively. Thus, the hinge topological phase transitions in our models can be characterized by the nested Wilson loop topological invariants.

- 
- [1] X.-L. Qi and S.-C. Zhang, *Rev. Mod. Phys.* **83**, 1057 (2011).
- [2] M. Z. Hasan and C. L. Kane, *Rev. Mod. Phys.* **82**, 3045 (2010).
- [3] L. Fu, C. L. Kane, and E. J. Mele, *Phys. Rev. Lett.* **98**, 106803 (2007).
- [4] L. Fu and C. L. Kane, *Phys. Rev. B* **76**, 045302 (2007).
- [5] H. Zhang, C.-X. Liu, X.-L. Qi, X. Dai, Z. Fang, and S.-C. Zhang, *Nat. Phys.* **5**, 438 (2009).
- [6] Y. L. Chen, J. G. Analytis, J.-H. Chu, Z. K. Liu, S.-K. Mo, X. L. Qi, H. J. Zhang, D. H. Lu, X. Dai, Z. Fang, S. C. Zhang, I. R. Fisher, Z. Hussain, and Z.-X. Shen, *Science* **325**, 178 (2009).
- [7] D. Hsieh, Y. Xia, D. Qian, L. Wray, F. Meier, J. H. Dil, J. Osterwalder, L. Patthey, A. V. Fedorov, H. Lin, A. Bansil, D. Grauer, Y. S. Hor, R. J. Cava, and M. Z. Hasan, *Phys. Rev. Lett.* **103**, 146401 (2009).
- [8] L. Fu and C. L. Kane, *Phys. Rev. Lett.* **100**, 096407 (2008).
- [9] C.-X. Liu and B. Trauzettel, *Phys. Rev. B* **83**, 220510(R) (2011).
- [10] J.-P. Xu, C. Liu, M.-X. Wang, J. Ge, Z.-L. Liu, X. Yang, Y. Chen, Y. Liu, Z.-A. Xu, C.-L. Gao, D. Qian, F.-C. Zhang, and J.-F. Jia, *Phys. Rev. Lett.* **112**, 217001 (2014).
- [11] J. Wang, Q. Zhou, B. Lian, and S.-C. Zhang, *Phys. Rev. B* **92**, 064520 (2015).
- [12] Q. L. He, L. Pan, A. L. Stern, E. C. Burks, X. Che, G. Yin, J. Wang, B. Lian, Q. Zhou, E. S. Choi, K. Murata, X. Kou, Z. Chen, T. Nie, Q. Shao, Y. Fan, S.-C. Zhang, K. Liu, J. Xia, and K. L. Wang, *Science* **357**, 294 (2017).

- [13] L. Fu and C. L. Kane, *Phys. Rev. Lett.* **102**, 216403 (2009).
- [14] A. R. Akhmerov, J. Nilsson, and C. W. J. Beenakker, *Phys. Rev. Lett.* **102**, 216404 (2009).
- [15] L. Fu and C. L. Kane, *Phys. Rev. B* **79**, 161408(R) (2009).
- [16] S. Mi, D. I. Pikulin, M. Wimmer, and C. W. J. Beenakker, *Phys. Rev. B* **87**, 241405(R) (2013).
- [17] C. W. J. Beenakker, P. Baireuther, Y. Herasymenko, I. Adagideli, L. Wang, and A. R. Akhmerov, *Phys. Rev. Lett.* **122**, 146803 (2019).
- [18] W. A. Benalcazar, B. A. Bernevig, and T. L. Hughes, *Phys. Rev. B* **96**, 245115 (2017).
- [19] W. A. Benalcazar, B. A. Bernevig, and T. L. Hughes, *Science* **357**, 61 (2017).
- [20] Z. Song, Z. Fang, and C. Fang, *Phys. Rev. Lett.* **119**, 246402 (2017).
- [21] J. Langbehn, Y. Peng, L. Trifunovic, F. von Oppen, and P. W. Brouwer, *Phys. Rev. Lett.* **119**, 246401 (2017).
- [22] F. Schindler, A. M. Cook, M. G. Vergniory, Z. Wang, S. S. P. Parkin, B. A. Bernevig, and T. Neupert, *Sci. Adv.* **4**, 0346 (2018).
- [23] M. Geier, L. Trifunovic, M. Hoskam, and P. W. Brouwer, *Phys. Rev. B* **97**, 205135 (2018).
- [24] F. Schindler, Z. Wang, M. G. Vergniory, A. M. Cook, A. Murani, S. Sengupta, A. Y. Kasumov, R. Deblock, S. Jeon, I. Drozdov, H. Bouchiat, S. Guérón, A. Yazdani, B. A. Bernevig, and T. Neupert, *Nat. Phys.* **14**, 918 (2018).
- [25] M. Ezawa, *Phys. Rev. Lett.* **120**, 026801 (2018).
- [26] E. Khalaf, *Phys. Rev. B* **97**, 205136 (2018).
- [27] C.-H. Hsu, P. Stano, J. Klinovaja, and D. Loss, *Phys. Rev. Lett.* **121**, 196801 (2018).
- [28] X. Zhu, *Phys. Rev. B* **97**, 205134 (2018).
- [29] L. Trifunovic and P. W. Brouwer, *Phys. Rev. X* **9**, 011012 (2019).
- [30] Y. Volpez, D. Loss, and J. Klinovaja, *Phys. Rev. Lett.* **122**, 126402 (2019).
- [31] X. Zhu, *Phys. Rev. Lett.* **122**, 236401 (2019).
- [32] Y. Xu, Z. Song, Z. Wang, H. Weng, and X. Dai, *Phys. Rev. Lett.* **122**, 256402 (2019).
- [33] C. Yue, Y. Xu, Z. Song, H. Weng, Y.-M. Lu, C. Fang, and X. Dai, *Nat. Phys.* **15**, 577 (2019).
- [34] X.-L. Sheng, C. Chen, H. Liu, Z. Chen, Z.-M. Yu, Y. X. Zhao, and S. A. Yang, *Phys. Rev. Lett.* **123**, 256402 (2019).
- [35] C. Chen, Z. Song, J.-Z. Zhao, Z. Chen, Z.-M. Yu, X.-L. Sheng, and S. A. Yang, *Phys. Rev. Lett.* **125**, 056402 (2020).
- [36] Y. Ren, Z. Qiao, and Q. Niu, *Phys. Rev. Lett.* **124**, 166804 (2020).
- [37] R.-X. Zhang, F. Wu, and S. Das Sarma, *Phys. Rev. Lett.* **124**, 136407 (2020).
- [38] B. Roy, *Phys. Rev. B* **101**, 220506(R) (2020).
- [39] M. Kheirkhah, Z. Yan, Y. Nagai, and F. Marsiglio, *Phys. Rev. Lett.* **125**, 017001 (2020).
- [40] M. Kheirkhah, Z. Yan, and F. Marsiglio, *Phys. Rev. B* **103**, L140502 (2021).
- [41] Z. Yan, F. Song, and Z. Wang, *Phys. Rev. Lett.* **121**, 096803 (2018).
- [42] Q. Wang, C.-C. Liu, Y.-M. Lu, and F. Zhang, *Phys. Rev. Lett.* **121**, 186801 (2018).
- [43] R.-X. Zhang, W. S. Cole, and S. Das Sarma, *Phys. Rev. Lett.* **122**, 187001 (2019).
- [44] L. Chen, B. Liu, G. Xu, and X. Liu, *Phys. Rev. Res.* **3**, 023166 (2021).
- [45] X. Wu, W. A. Benalcazar, Y. Li, R. Thomale, C.-X. Liu, and J. Hu, *Phys. Rev. X* **10**, 041014 (2020).
- [46] X.-H. Pan, K.-J. Yang, L. Chen, G. Xu, C.-X. Liu, and X. Liu, *Phys. Rev. Lett.* **123**, 156801 (2019).
- [47] X. Wu, X. Liu, R. Thomale, and C.-X. Liu, *Nat. Sci. Rev. nwab087* (2021), doi: 10.1093/nsr/nwab087.
- [48] R.-X. Zhang, W. S. Cole, X. Wu, and S. Das Sarma, *Phys. Rev. Lett.* **123**, 167001 (2019).
- [49] Y. Peng and Y. Xu, *Phys. Rev. B* **99**, 195431 (2019).
- [50] Y.-J. Wu, J. Hou, Y.-M. Li, X.-W. Luo, X. Shi, and C. Zhang, *Phys. Rev. Lett.* **124**, 227001 (2020).
- [51] S.-B. Zhang, A. Calzona, and B. Trauzettel, *Phys. Rev. B* **102**, 100503(R) (2020).
- [52] S.-B. Zhang, W. B. Rui, A. Calzona, S.-J. Choi, A. P. Schnyder, and B. Trauzettel, *Phys. Rev. Res.* **2**, 043025 (2020).
- [53] K. Laubscher, D. Loss, and J. Klinovaja, *Phys. Rev. Research*, **2**, 013330 (2020).
- [54] B.-X. Li and Z. Yan, *Phys. Rev. B* **103**, 064512 (2021).
- [55] S. Qin, L. Hu, X. Wu, X. Dai, C. Fang, F.-C. Zhang, and J. Hu, *Sci. Bull.* **64**, 1207 (2019).
- [56] X. Wu, S. Qin, Y. Liang, H. Fan, and J. Hu, *Phys. Rev. B* **93**, 115129 (2016).
- [57] G. Xu, B. Lian, P. Tang, X.-L. Qi, and S.-C. Zhang, *Phys. Rev. Lett.* **117**, 047001 (2016).
- [58] P. Zhang, K. Yaji, T. Hashimoto, Y. Ota, T. Kondo, K. Okazaki, Z. Wang, J. Wen, G. D. Gu, H. Ding, and S. Shin, *Science* **360**, 182 (2018).
- [59] D. Wang, L. Kong, P. Fan, H. Chen, S. Zhu, W. Liu, L. Cao, Y. Sun, S. Du, J. Schneeloch, R. Zhong, G. Gu, L. Fu, H. Ding, and H.-J. Gao, *Science* **362**, 333 (2018).
- [60] X.-L. Qi, T. L. Hughes, and S.-C. Zhang, *Phys. Rev. B* **81**, 134508 (2010).
- [61] F. Zhang, C. L. Kane, and E. J. Mele, *Phys. Rev. Lett.* **111**, 056402 (2013).
- [62] A. Haim and Y. Oreg, *Physics Reports* **825**, 1 (2019).
- [63] A. P. Schnyder, S. Ryu, A. Furusaki, and A. W. W. Ludwig, *Phys. Rev. B* **78**, 195125 (2008).
- [64] S. Ryu, A. P. Schnyder, A. Furusaki, and A. W. W. Ludwig, *New J. Phys.* **12**, 065010 (2010).
- [65] C.-K. Chiu, J. C. Y. Teo, A. P. Schnyder, and S. Ryu, *Rev. Mod. Phys.* **88**, 035005 (2016).
- [66] See Appendices for a detailed description of the topology of the (010) surface, comparison with the HMHMs phase based on strong TI and trivial insulator, the coexistence of HMHMs and CMHMs, other higher-order TI or TSC models based on weak TIs, the numerical calculations of the Wilson loop and nested Wilson loop.
- [67] B. Bernevig and T. Hughes, *Topological Insulators and Topological Superconductors* (Princeton University Press, Princeton, NJ, 2013).
- [68] X.-L. Qi, T. L. Hughes, and S.-C. Zhang, *Phys. Rev. B* **78**, 195424 (2008).
- [69] K. Luo, H. Geng, L. Sheng, W. Chen, and D. Y. Xing, *Phys. Rev. B* **104**, 085427 (2021).
- [70] C.-A. Li, S.-B. Zhang, J. Li, and B. Trauzettel, *Phys. Rev. Lett.* **127**, 026803 (2021).
- [71] J. C. Y. Teo and C. L. Kane, *Phys. Rev. B* **82**, 115120 (2010).
- [72] A. Y. Kitaev, *Phys. Usp.* **44**, 131 (2001).

- [73] P. Ghosh, J. D. Sau, S. Tewari, and S. Das Sarma, *Phys. Rev. B* **82**, 184525 (2010).
- [74] B. van Heck, A. R. Akhmerov, F. Hassler, M. Burrello, and C. W. J. Beenakker, *New J. Phys.* **14**, 035019 (2012).
- [75] X. Liu, X. Li, D.-L. Deng, X.-J. Liu, and S. Das Sarma, *Phys. Rev. B* **94**, 014511 (2016).
- [76] R. Noguchi, T. Takahashi, K. Kuroda, M. Ochi, T. Shirasawa, M. Sakano, C. Bareille, M. Nakayama, M. D. Watson, K. Yaji, A. Harasawa, H. Iwasawa, P. Dudin, T. K. Kim, M. Hoesch, V. Kandyba, A. Giampietri, A. Barinov, S. Shin, R. Arita *et al.*, *Nature (London)* **566**, 518 (2019).
- [77] R. Wu, J.-Z. Ma, S.-M. Nie, L.-X. Zhao, X. Huang, J.-X. Yin, B.-B. Fu, P. Richard, G.-F. Chen, Z. Fang, X. Dai, H.-M. Weng, T. Qian, H. Ding, and S. H. Pan, *Phys. Rev. X* **6**, 021017 (2016).
- [78] X.-B. Li, W.-K. Huang, Y.-Y. Lv, K.-W. Zhang, C.-L. Yang, B.-B. Zhang, Y. B. Chen, S.-H. Yao, J. Zhou, M.-H. Lu, L. Sheng, S.-C. Li, J.-F. Jia, Q.-K. Xue, Y.-F. Chen, and D.-Y. Xing, *Phys. Rev. Lett.* **116**, 176803 (2016).
- [79] S. Liu, M. X. Wang, C. Chen, X. Xu, J. Jiang, L. X. Yang, H. F. Yang, Y. Y. Lv, J. Zhou, Y. B. Chen, S. H. Yao, M. H. Lu, Y. F. Chen, C. Felser, B. H. Yan, Z. K. Liu, and Y. L. Chen, *APL Mater.* **6**, 121111 (2018).
- [80] J. Hyun, M. Y. Jeong, S. Kim, M.-C. Jung, Y. Lee, C.-y. Lim, J. Cha, G. Lee, Y. An, M. Hashimoto, D. Lu, J. D. Denlinger, M. J. Han, and Y. Kim, [arXiv:2009.05917](https://arxiv.org/abs/2009.05917).
- [81] L. X. Xu, Y. Y. Y. Xia, S. Liu, Y. W. Li, L. Y. Wei, H. Y. Wang, C. W. Wang, H. F. Yang, A. J. Liang, K. Huang, T. Deng, W. Xia, X. Zhang, H. J. Zheng, Y. J. Chen, L. X. Yang, M. X. Wang, Y. F. Guo, G. Li, Z. K. Liu *et al.*, *Phys. Rev. B* **103**, L201109 (2021).
- [82] G. Dhakal, M. Mofazzel Hosen, A. Ghosh, C. Lane, K. Gornicka, M. J. Winiarski, K. Dimitri, F. Kabir, C. Sims, S. Regmi, W. Neff, L. Persaud, Y. Liu, D. Kaczorowski, J.-X. Zhu, T. Klimczuk, and M. Neupane, [arXiv:1911.08519](https://arxiv.org/abs/1911.08519).
- [83] H. Zhang, A. Rousuli, S. Shen, K. Zhang, C. Wang, L. Luo, J. Wang, Y. Wu, Y. Xu, W. Duan, H. Yao, P. Yu, and S. Zhou, *Sci. Bull.* **65**, 188 (2020).
- [84] X. Wu, S. Qin, Y. Liang, C. Le, H. Fan, and J. Hu, *Phys. Rev. B* **91**, 081111(R) (2015).
- [85] M. Gray, J. Freudenstein, S. Y. F. Zhao, R. O'Connor, S. Jenkins, N. Kumar, M. Hoek, A. Kopec, S. Huh, T. Taniguchi, K. Watanabe, R. Zhong, C. Kim, G. D. Gu, and K. S. Burch, *Nano Lett.* **19**, 4890 (2019).
- [86] T. Morimoto and A. Furusaki, *Phys. Rev. B* **89**, 035117 (2014).
- [87] C.-K. Chiu, [arXiv:1410.1117](https://arxiv.org/abs/1410.1117).